Accepted Manuscript

Volume 46
Number 10
14 March 2017
Pages 3073-3412

Dalton Transactions

An international journal of inorganic chemistry

rsc.li/dalton

COMMUNICATION
Douglas W. Stephen et al
N-Heterocyclic carbene stabilized parent sulfenyl, selenenyl,
and tellurenyl cations (XH⁺, X = S, Se, Te)

ISSN 0306-0012

ROYAL SOCIETY
OF CHEMISTRY

ROYAL SOCIETY
OF CHEMISTRY

rsc.li/dalton

Dalton Transactions

ARTICLE

Bio-Inspired copper complexes with Cu$_2$S cores: (solvent)effects on oxygen reduction reactions.

Jordan Mangue,[a] Iris Wehrung,[b] Jacques Pécaut,[c] Stéphane Ménage,[a] Maylis Orio*[b] and Stéphane Torelli*[a]

The need for effective alternative energy sources and "green" industrial processes is more than ever a societal topic. In this context, mastering the Oxygen Reduction Reactions (ORR) is a key step to develop fuel cells or to propose alternatives to energy-intensive setups such as the anthraquinone process for hydrogen peroxide production. Achieving this goal using bio-inspired metal complexes based on abundant and non-toxic elements could provide an environmentally friendly option. Given the prevalence of Cu-containing active sites capable of reductive activation of dioxygen in Nature, the development of Cu-based catalysts for ORR thus appears to be a relevant approach. We herein report the preparation, full characterization and (TD)DFT investigation of a new dinuclear mixed-valent copper complex **6** exhibiting a Cu$_2$S core and a bridging triflate anion. Its ORR activity is compared with that of its parent catalyst **1**. Two types of solvents are used, acetonitrile or acetone, and various catalyst/Me$_8$Fc (electron source) ratios are tested. Our results highlight a counterintuitive solvent effect for **1** and a drastic drop of activity for **6** in coordinating acetonitrile along with modification of its chemical structure.

Introduction

Oxygen Reduction Reactions (ORR) gather the reduction of dioxygen (O$_2$) into hydrogen peroxide (O$_2$ + 2e$^-$ + 2H$^+$ → H$_2$O$_2$) and water (O$_2$ + 4e$^-$ + 4H$^+$ → 2H$_2$O).[1] On one hand, reduction into H$_2$O takes place into conventional fuel cells and is an efficient method for converting chemical energy (stored in the O=O bond) into electrical one. Unfortunately, the most powerful systems remain those based on noble metal-containing architectures.[2, 3] One the other hand, H$_2$O$_2$ is a well-known reagent (part of the 100 most important chemicals used)[4, 5] for various industrial purposes (aqueous and organic media). It applies for water treatment,[6] paper bleaching,[7] disinfection,[8] chips making processes[9] and aerospace.[10] It is also considered as the prototype of green oxidant for organic synthesis[11]. More recently, its propensity to be utilized in mono-compartmental fuel cells has emerged.[12] The consequence is an increase of the worldwide demand that should reach 5.7 million tons by 2027.[13] More than 95 % of the global H$_2$O$_2$ production comes from the so-called anthraquinone (or Reidel-Pfederer) process. This method is energy consuming, dangerous (use of H$_2$ and O$_2$, transportation), produces a lot of waste and requires noble-based metal (Pt, Pd) catalysts.[14] Given that, it becomes clear that providing efficient, environmentally friendly and on-site selective ORR catalysts is a crucial to fulfill future needs and applications. This is particularly the case when considering a use for organic synthesis that requires "water-free" environments.

O$_2$ activation being one of the most important processes used by Nature to fulfill vital metabolic functions, bio-inorganic chemists have investigated this field by the means of bio-inspired or biomimetic complexes based on abundant and non-toxic transition metal ions such as Fe and Mn.[15] Mono and dinuclear Cu-containing complexes are also reported for efficient O$_2$ activation.[16] When dealing specifically with ORR, the electron supply can be achieved by an electrode. Generally, H$_2$O production is mainly favored.[17-23] Extensive and deep mechanistic investigations provided undeniable insights on the role of the solvent(s) or proton source(s) in the reactivity.[24-28] The use of sacrificial chemical electron sources such as ferrocene derivatives is an alternative. In this case, interesting results are obtained even if the activity in terms of turnover frequencies for instances (TOFs) cannot compete with electrocatalysis. However, H$_2$O$_2$ production can be obtained under given conditions.[23, 29] In this line, we previously described the unique behavior of the dinuclear mixed valent (MV) complex **1** (Fig. 1)[30] that proves, in acetonitrile, to be selective either for H$_2$O$_2$ or H$_2$O depending on the amount of octamethyl or decamethylferrocene (Me$_8$Fc or Me$_{10}$Fc) present in the medium. In all cases, reactions are extremely fast when dealing with homogeneous catalysis (TOF ~ 10 s^{-1}), with full consumption of the ferrocene derivative.[31]

Driven by the hypothesis that the unique reactivity of **1** could be related to its N$_3$S environment and the presence of a Cu-Cu bond, we prepared a new MV copper complex having a N$_2$S motif. This will open the Cu coordination sphere(s) to exogenous ligands such as counter-anions and/or solvent molecules. Consequently, complex **6** featuring a ligated OTf$^-$ (OTf$^-$ = trifluoromethanesulfonate anion) was isolated and fully characterized. The structural differences between **1** and **6** finally allowed to investigate their abilities for ORR either in non-coordinating acetone or in coordinating acetonitrile (Figure 1). The results of this work clearly demonstrate the influence of the Cu environment on the reactivity in terms of selectivity, kinetics and solvent tolerance of the reaction.

[a.] Univ. Grenoble Alpes, CNRS, CEA, IRIG, Laboratoire de Chimie et Biologie des Métaux, 17 rue des Martyrs, 38054 Grenoble Cedex 9, France.
[b.] Aix Marseille Univ. Centrale Med., ISM2, Marseille, France.
[c.] Univ. Grenoble Alpes, CEA, CNRS, IRIG, SYMMES, UMR 5819, F-38000 Grenoble, France.

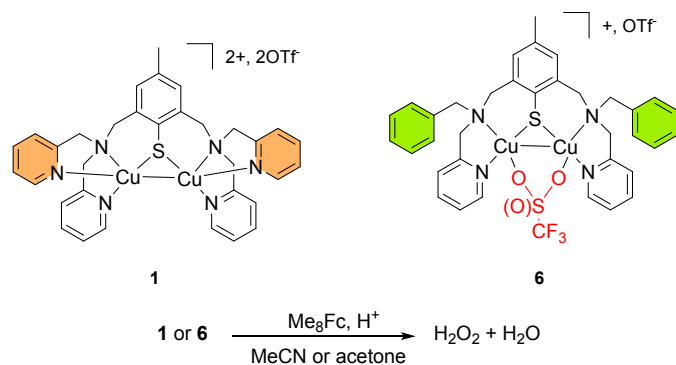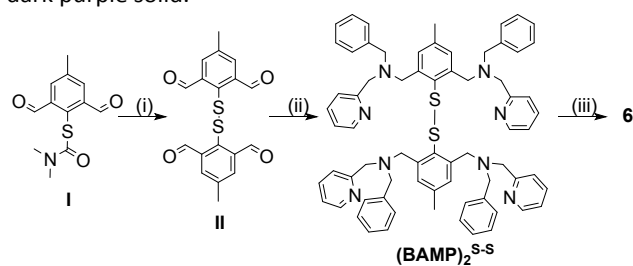**Dalton Transactions Accepted Manuscript**

ARTICLE

Fig. 1 Chemical representations of **1**,[30] **6** and targeted ORR.

Results and discussion

Preparation and characterization of 6.

The synthesis of the (**BAMP**)$_2$$^{S-S}$ ligand (Figure 2 and ESI for experimental details) slightly differs from the ones we already reported for the preparation of other disulfides-containing derivatives.[30, 32] This time, deprotection of the key methyl-diformyl-S-thiocarbamate precursor **(I)** is achieved under mild conditions (NaOH 1 M instead of LiAlH$_4$ or concentrated KOH and heating) and dimerization into the disulfide performed using iodine. Subsequent reductive amination with [(benzyl-amino)methyl]pyridine and sodium triacetoxyborohydride finally gives the title ligand. Metalation with four molar eq. of [Cu(CH$_3$CN)$_4$](OTf) in acetone results in the isolation of **6** as a dark purple solid.

(i) NaOH 1 M then I$_2$; (ii) [(benzylamino)methyl]pyridine, NaH[B(OAc)$_3$]; (iii) [Cu(CH$_3$CN)$_4$](OTf)

Fig. 2. Preparation of the (BAMP)$_2$$^{S-S}$ ligand from **(I)**[30] and metalation into **6**.

The ESI-MS of **6** in acetone (Figure S1, ESI) displays isotopic patterns at m/z = 671.1, 820.0 and 968.9 corresponding to mono-charged ions ([BAMP^S + 2Cu]$^+$, [BAMP^S + 2Cu + 1 OTf]$^+$, [BAMP^S + 2Cu + 2 OTf]$^+$, respectively) that attest for the presence of the Cu$_2$S core as well as for the integrity of the ligand. Crystals suitable for X-ray analysis are obtained upon layering pentane upon an acetone solution of the complex. As already observed for other members of the series,[30, 32, 33] reductive cleavage of the S-S bond occurs and leads to the formation of a MV(II,I) dinuclear species (Figure 3). Both metal centers are pentacoordinated by the N/S atoms from the ligand, a O-atom from a triflate anion and the neighboring Cu. The Cu1-O1S2 = 2.176 (2) Å and Cu2-O2S2 = 2.674 (9) Å bond distances clearly indicate a weak bridging interaction. A Cu-Cu bond of 2.5475(5) Å is present and will be further confirmed by theoretical calculations. When comparing **6** with **1** and focusing

on the Cu$_2$S core, the metrics are relatively close with Cu1-Cu2 = 2.5762(12), Cu1-S = 2.177(2) and Cu2-S = 2.193(2) for the latter.

Density Functional Theory (DFT) calculations were then performed to investigate the structure and properties of **6** and support the experimental findings. The complex was first subjected to geometry optimization in implicit solvent for comparison with the solid-state structure (Figure 4). The main result is that the integrity of the structure remains. The computed Cu1-S1, Cu2-S1, Cu1-N1, Cu1-N2, Cu2-N3 and Cu2-N4 bond distances of 2.211, 2.207, 2.133, 1.986, 2.140 and 1.983 Å indeed fall in the range of the experimental ones. Looking more specifically at the Cu1-Cu2 motif, a deviation between the computed (2.719 Å) and the experimental (2.5475(5) Å) metal-metal bond distance is observed. Finally, a significant shortening of one of the two Cu-OTf bonds (from 2.674(9) to 2.397 Å) is obtained that somehow renders the binding mode of the OTf anion more symmetrical. This can be tentatively attributed to the relaxation of the complex upon geometry optimization in solvated medium, as opposed to the frozen X-ray (solid-state) structure. This finding suggests that particular attention will have to be paid when conducting the computational modeling, since it may have repercussions on the calculated (UV-Vis/NIR, EPR and redox) properties.
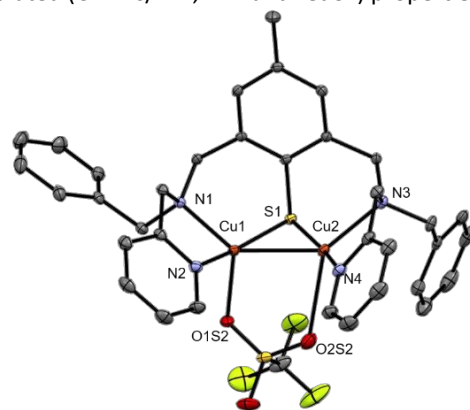

Fig. 3 ORTEP diagram (30 % probability) for the dicationic unit of **6**. H-atoms are omitted for clarity. Selected bond distances (Å): Cu1-Cu2 2.5475(5), Cu1-S1 2.1798(8), Cu2-S1 2.1661(8), Cu1-N1 2.043(2), Cu1-N2 1.959(3), Cu1-O1S2 2.176(2), Cu2-N3 2.114(3), Cu2-N4 1.945(3), Cu2-O2S2 2.674(9); see Tables S1-S3, ESI.

Insight into the Cu-Cu bond is obtained by Natural Bond Order (NBO) analysis using the DFT-optimized structure of **6** (Figure S2 and Table S4, ESI). The calculated Wiberg bond index of 0.54 compares quite well with the one obtained for **1** (0.40), thus supporting the presence of a metal-metal bond. The relevant occupied natural orbital representing this Cu-Cu motif corresponds to a σ (4p3d/4p3d) overlap between the two metal centers. Note that a similar orbital was also found from calculations using the X-ray crystal structure featuring a shorter Cu-Cu distance of 2.5475(5) Å (Figure S3 and Table S4, ESI). Electronic structure calculations using the DFT-optimized structure of **6** provide a singly occupied molecular orbital (SOMO) that is predominantly metal-based and features 30, 27 and 20 % contributions from the Cu1, Cu2 and S centers, respectively (Figure S4, ESI). Mulliken population analysis (Figure S4 and Table S5, ESI) shows that the spin density is

equally distributed between the two copper centers and the coordinating sulfur, which strongly suggests that **6** is a fully delocalized ($Cu^{1.5}Cu^{1.5}$) MV species.
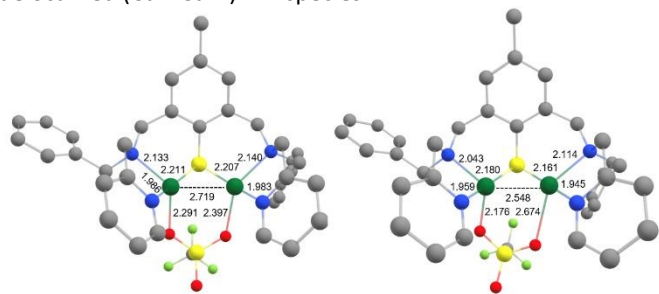

Fig. 4 Comparison of DFT-optimized geometry of **6** (left) and X-ray solid-state structure (right). H-atoms are omitted for clarity. Color scheme: Cu olive green, S yellow, O red, N dark blue, F light green, C light grey.

The electronic properties of **6** were then investigated in acetone. The X-band EPR spectrum recorded at 10 K (Figure 5(A)) exhibits a complicated multiline pattern, as already observed for **1** and attributed to a ($Cu^{1.5}Cu^{1.5}$) MV state. This is further confirmed since the simulated spectrum (Figure 5(A)) using the computed parameters obtained with the DFT-optimized structure with a fully delocalized valence (Table S6, ESI) adequately reproduces the main experimental features. In the same vein, the UV-Vis/NIR absorption spectrum (Figure 5(B)) displays intense and well-defined absorption bands that reminds those of **1** in acetone. The near-infrared feature at 1285 nm (ε = 1025 $M^{-1}.cm^{-1}$) is thus assigned to intervalence charge transfer transitions (IVCT) and the others at 780 nm (ε = 1245 $M^{-1}.cm^{-1}$) and 560 nm (ε = 605 $M^{-1}.cm^{-1}$) to ligand-to-metal charge transfer (LMCT) transitions. These attributions are corroborated by TD-DFT calculations since three main absorption bands at 481 nm, 703 nm and 1255 nm are indeed obtained (Figure 5(B), Figure S5 and Table S7, ESI).
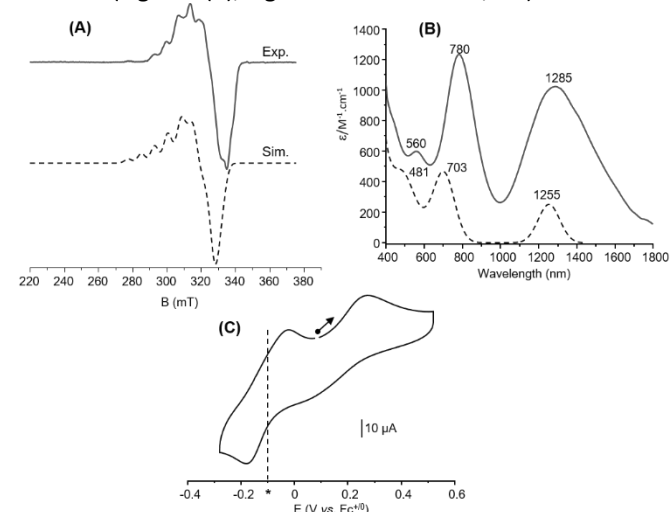

Fig. 5 Characterization of **6** in acetone: (A) Experimental (solid line, 10 K, 0.67 mM with microwave freq. 9.40 GHz; power 0.25 mW; mod. ampl. 1 mT; freq. 100 kHz) and Easyspin-simulated (dashed line) X-band EPR spectra, (B) Experimental (solid line) and TD-DFT-calculated (dashed line) UV-Vis/NIR spectra and (C) Cyclic voltammogram (0.7 mM) in acetone with 0.1 M $TBAPF_6$ as supporting electrolyte and glassy carbon as working electrode. The curve corresponds to the initial scan at 100 $mV.s^{-1}$ starting from the open-circuit potential and (*) indicates the standard potential obtained by DFT calculations.

Interestingly, the TD-DFT-computed UV-Vis/NIR spectrum using the X-ray crystal structure (Figure S6 and Table S8, ESI) exhibits

two main absorption bands predicted at 1007 nm and 613 nm. Although far from the experimental values, these signatures are, however, similar to those obtained when recording the solid-state spectrum of **6** diluted in $BaSO_4$ (Figure S6, ESI) with bands at 1005 nm and 605 nm. This result reinforces the finding that solvation has repercussions on the complex geometry once solubilized.

Finally, the CV curve displays two distinct redox processes (Figure 5(C)) when starting at the open-circuit potential (OCP) towards the anodic direction. The first one at E_{pa} = 0.27 V vs. $Fc^{+/0}$ is irreversible and attributed to $Cu^{II}Cu^{I} \to Cu^{II}Cu^{II}$. The second one observed at -0.10 V vs $Fc^{+/0}$ (E_{pa} = -0.02 V, E_{pc} = -0.18 V, ΔE_p = 0.16 V) is quasi reversible and corresponds to $Cu^{II}Cu^{I} \to Cu^{I}Cu^{I}$. DFT calculations (optimized structure) provide a computed redox potential of -0.102 V vs $Fc^{+/0}$ for the cathodic region that matches the experimental data (Tables S9-S10, ESI) and support the above assignment. The irreversibility of the anodic part clearly indicates structural changes at the metal coordination sphere(s) that stabilizes the *in situ* generated dicopper(II) state. No noticeable changes occur on the reversibility when performing a CV scan towards the cathodic direction from the OCP (Figure S7, ESI) One can note that a reversible oxidation process was on the contrary evidenced for **1**.

Altogether, this set of experimental and theoretical data is in favor of the structure of **6** being retained in acetone. What also emerges, and needs to be emphasized, is that the DFT-optimized structure is here perfectly adapted to describe the conformation and the electronic properties of **6** in solution.

Catalytic O_2 reduction by 1 and 6 with Me_8Fc and lutidinium tetrafluoroborate (LutH)

We already showed that **1** is capable of ORR in coordinating MeCN, its structure being maintained in this solvent as it is in non-coordinating acetone.[31] Selectivity (H_2O_2 vs. H_2O) is achieved by controlling the relative excess of the sacrificial electron source (Me_8Fc) compared to the Cu catalyst in the presence of lutidinium tetrafluoroborate (LutH) as chemically innocent proton source. With **6** in hands and its coordination sphere sensibly different from that of **1**, comparing the ORR abilities of both catalysts in MeCN or acetone could provide insights into the parameters at stake for orienting the selectivity. The experimental conditions are the same as those already used for **1** in MeCN. First, the ORR activity of **1** in acetone was investigated. The results (Table 1 and Table S11, ESI) indicate, as already observed in MeCN, that Me_8Fc is entirely consumed for each condition since the expected absorbance values for full Me_8Fc^+ accumulation at $\lambda_{maxMe8Fc+}$ = 750 nm (ε = 460 $M^{-1}.cm^{-1}$ in acetone) are experimentally obtained (Figure 6(A) and Figures S8(A)-S10, ESI). Interestingly, kinetics are longer compared to those previously determined in MeCN. Considering that coordinating solvents such as MeCN usually slow down the reactivity, this quite counterintuitive result could indicate that no labile position(s) are available for MeCN at the metal coordination sphere(s) during catalysis.
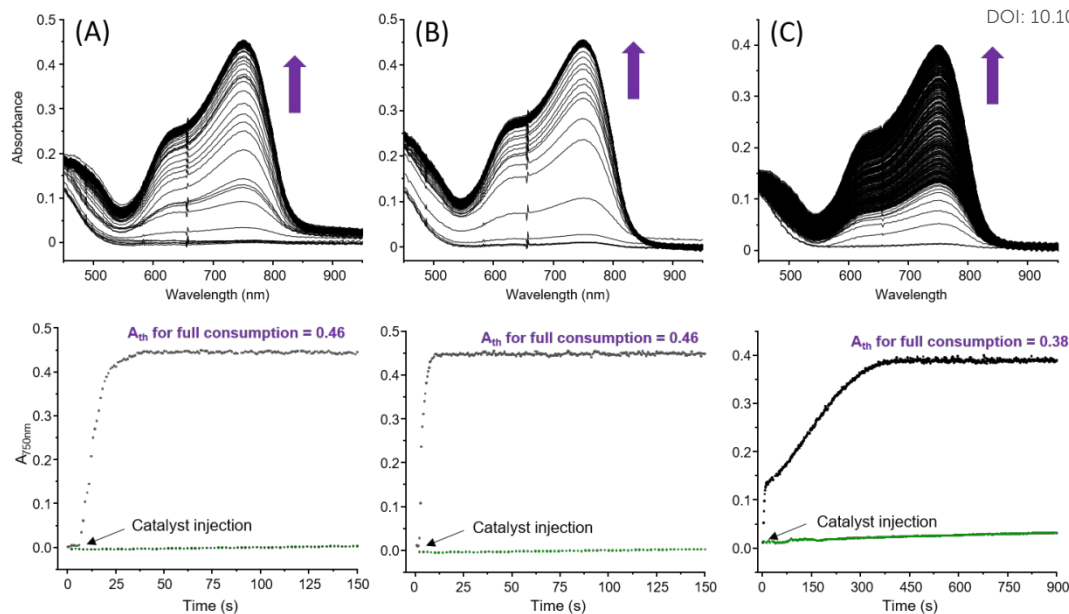
Fig. 6 Selected UV-vis absorption spectral changes and time dependence recorded at 785 nm corresponding to the accumulation of Me_8Fc^+ during ORR performed in saturated O_2-solutions using Cu catalysts (0.05 mM), Me_8Fc (2 mM) and LutH (20 mM) corresponding to 1/20/400 molar eq. for **1** in acetone (A); **6** in acetone (B) and **6** in MeCN (C) at 298 K. The black arrows indicate the injection of the catalyst in the reaction mixture containing pre-incubated Me_8Fc and LutH. In each case, the blank experiment using commercial $[Cu(CH_3CN)_4](OTf)$ is shown with the green trace.

In large Me_8Fc excess, a model with two k_{obs} values is required, suggesting however chemical changes at the catalyst within time in the reaction mixture that also contains accumulated O_2-reduced species. Second, the ORR activity of **6** was studied in MeCN ($\lambda_{maxMe8Fc+}$ = 750 nm, ε = 390 $M^{-1}.cm^{-1}$) and acetone (Figure 6(B) and 6(C)). In acetone, full Me_8Fc consumption also occurs (Table 1, Figures S8(B), S11-12 and Table S11, ESI). Reaction rates and times are roughly independent of $[Me_8Fc]$. An average value of 14 s is calculated that makes **6** slower than **1** at low Me_8Fc concentrations (*i.e.* from 1/10/400 to 1/40/400, Cat/Me_8Fc/LutH, Table S11, ESI) but more efficient at high Me_8Fc concentrations (*i.e.* from 1/60/400, Cat/Me_8Fc/LutH, Table S11, ESI). A drastic change is observed in MeCN (Table 1, Figures S8(C), S13-S14 and Table S11, ESI). Whereas the reaction is complete up to 40 molar eq. of Me_8Fc within a longer but still acceptable timescale, very slow kinetics are obtained from 60 molar eq. to 100 molar eq. In these cases, the TON_{max} values are not even reached after 6000 s. This time, all the kinetic traces clearly indicate two different regimes: a "fast" one and a second, slower, suggesting that the catalyst evolves during the reaction towards a less reactive species (slow poisoning). One can also note that a factor of 10 for the reaction time is obtained between 20 molar eq. and 40 molar eq. Considering all these kinetic data, one might also note a rather unexpected trend for the k_{obs} values for **1** that decrease when increasing the amount of Me_8Fc. This negative order has to be opposed to the zero-order obtained for **6** in acetone (reactivity independent of $[Me_8Fc]$). The former may correlate with a less efficient outer sphere electron transfer (steric hindrance at the metal centres) that slower the reactivity as already invoked for dinuclear Mn

species.[34] Then, the selectivity of both complexes was evaluated via H_2O_2 titration (Table S1 and Table S11, ESI) with a dedicated Ti-based porphyrin (Figure S15, ESI).[35, 36] In acetone, **1** mainly produced H_2O_2 when using low Me_8Fc loadings, as already observed in MeCN. In acetone, **6** is rather unselective at low $[Me_8Fc]$ compared to **1**, as it is the case when switching to MeCN (34 % maximum). For both complexes, H_2O remains the main product for large Me_8Fc excess. Finally, looking at the TOFs, values between 1.5 s^{-1} and 17.6 s^{-1} at best are obtained. This result is rather modest compared to the huge efficiency usually obtained under homogeneous electrocatalytic conditions for reported copper complexes[25, 28, 37-40] and in the same range as those reported by Fukuzumi with stopped-flow experiments for the study of the well-known mononuclear $[(tmpa)(Cu^{II})(ClO_4)_2]$ species.[17]

The behavior observed for **6** in MeCN urged us to probe its chemical structure in this solvent for comparison with acetone. Noticeable changes occur on the UV-Vis/NIR and EPR spectra, as well as on the CV (Figure 7). The well-defined and intense absorption bands observed in acetone gave way to a featureless spectrum with no band in the NIR region that suggests a change in the valence state from mixed to localized (Figure 7(A)). This is in line with the EPR spectrum that turns to become characteristic of a mononuclear Cu(II) complex with axial symmetry (four lines pattern; I_{Cu}= 3/2, $2nI$ + 1 = 4 with n = 1, Figure 7(B)). Finally, even if the CV (Figure 7(C)) curve resembles the one recorded in acetone, a non-negligible cathodic shift occurs for the $Cu^{II}Cu^{I} \rightarrow Cu^{I}Cu^{I}$ process from to -0.10 V to -0.22 V vs. $Fc^{+/0}$ (E_{pa} = -0.18 V, E_{pc} = -0.26 V, ΔEp = 0.08 V) and a slight one (0.05 V) is detected for $Cu^{II}Cu^{I} \rightarrow Cu^{II}Cu^{II}$ (from E_{pa} = 0.27 V

Dalton Transactions Accepted Manuscript

Journal Name

ARTICLE

vs. Fc$^{+/0}$ to E$_{pa}$ = 0.22) that remains irreversible. The important result here is that the Cu^{II}Cu^{I} → Cu^{I}Cu^{I} event remains accessible by Me$_8$Fc to perform ORR. As observed in acetone, a similar CV curve is obtained when scanning towards the cathodic region (Figure S16, ESI). Additionally, the smaller ΔEp in MeCN (70 mV to 90 mV) compared to that observed in acetone (130 mV to 180 mV) for this scan rate-dependent redox event (Figure S15 in the ESI) also points out different electron transfer efficiencies that could have consequences on the activity. Electron self-exchange rate constants for **6** in both solvents were consequently determined by means of CV experiments (Figures S17 and S18, ESI). k$_{el}$ values of 1.5(1) 10^{-3} cm s^{-1} and 1.1(1) 10^{-2} cm s^{-1} (or estimated as k$_{hom}$ = 2.3(2) 10^5 L mol^{-1} s^{-1} and 1.67(6)·10^6 L mol^{-1} s^{-1}) are obtained in acetone and MeCN, respectively, indicating a faster electron transfer in MeCN and consistent with the ΔEp values. This result also suggests that this parameter is not directly related to the trend observed for ORR and the k$_{obs}$ values. Given these preliminary data, it is clear that **6** exists at different valence states/chemical structures when solvated in acetone or in MeCN. These changes have sufficient repercussions on the nature of the coordination sphere and the electronics so that the ORR activity is affected in terms of kinetics and/or selectivity. Indeed, for the 1/40/400 condition, **6** turns to be 250 times faster in acetone compared to MeCN (13.8 s *vs.* 3500 s for full Me$_8$Fc consumption, Table S11 in the ESI).
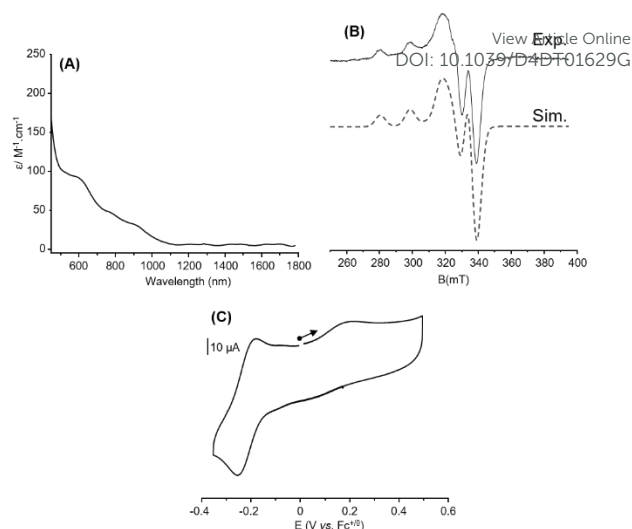

Fig. 7. Characterization of **6** in MeCN: (A) UV-Vis/NIR and (B) X-band EPR spectra (solid line, 10K, 0.5 mM with microwave freq. 9.41 GHz; power 0.25 mW; mod. ampl. 1 mT; freq. 100 kHz) and SimFonia simulation (dashed line) with g1 =2.041, g2 = 2.043, g3 = 2.18 , A1 = 57 MHz, A2= 86 MHz and A3 = 550 MHz; (C) CV (0.6 mM) in MeCN with 0.1 M TBAPF$_6$ as supporting electrolyte and glassy carbon as working electrode. The curve corresponds to the initial scan at 100 mV.s^{-1} starting from the open-circuit potential.

Table 1. Selected ORR experiments performed with **1** and **6** in air-saturated acetone or MeCN at room temperature using Me$_8$Fc and LutHBF$_4$ as electron and proton sources. The values obtained for **1** in MeCN (already reported)[31] are listed for comparison. See the supporting information for experimental details and Table S11 for full data.

Entry	[Me$_8$Fc] (mM)	Cat/e$^-$/H$^+$	TON	TON$_{max}$	k$_{obs}$ (s^{-1})	t (s)	% H$_2$O$_2$ Me$_8$Fc	% H$_2$O Me$_8$Fc	TOF (s^{-1})[b]
1 in MeCN[31]	0.5	1/10/400	10	10	1.06 ± 0.02	4.1 ± 0.2	90	10	5.3 ± 0.3
	3.0	1/60/400	60	60	0.13 ± 0.01	28.1 ± 0.5	51	49	8.3 ± 0.3
	5.0	1/100/400	100	100	0.12 ± 0.01	41.2 ± 2	10	90	14.1± 0.4
1 in acetone	0.5	1/10/400	10	10	0.30 ± 0.05	22.0 ± 0.8	70	30	1.5 ± 0.2
	3.0	1/60/400	60	60	0.05 ± 0.004	91 ± 4	31	69	1.9 ± 0.2
	5.0	1/100/400	100	100	0.10 ± 0.02 0.014 ± 0.009	268 ± 10	20	80	2.7 ± 0.4
6 in acetone	0.5	1/10/400	10	10	0.51 ± 0.01	11.2 ± 0.9	42	54	3.1 ± 0.2
	3.0	1/60/400	60	60	0.40 ± 0.004	15.1 ± 1.2	11	89	10.6 ± 0.4
	5.0	1/100/400	100	100	0.46 ± 0.006	15.5 ± 1.3	5	95	17.6 ± 0.2
6 in MeCN	0.5	1/10/400	10	10	0.51 ± 0.05 89.9 ± 8	340 ± 30	34	66	< 1
	3.0	1/60/400	50[a]	60	nd	> 6000	nd	nd	nd
	5.0	1/100/400	40[a]	100	nd	> 6000	nd	nd	nd

(a) after 6000 s reaction time; *nd*: not determined; (b) determined for the first kinetic event in the case of multi regimes.

Conclusion

To conclude, we report here the preparation, full characterization and ORR activity of a new MV dicopper complex **6** that is compared to its parent catalyst **1**. Both complexes contain a Cu$_2$S MV core but differ by the number of coordinating atoms from the ligands. In the case of **6**, this leads to the presence of potentially exchangeable position(s) Theoretical investigations nicely demonstrate that special attention must be paid on the use of an optimized *vs.* X-ray

structure to probe electronic properties. In our case, the former is more suitable. From a reactivity point of view, significant differences on the kinetics and selectivity for ORR (k$_{obs}$ and reaction times) are obtained. **1** remains the most selective catalyst since a control of the amount of the sacrificial electron source allows to swing from H$_2$O$_2$ to H$_2$O as the main product. **6** does not exhibit such a pronounced selectivity but appears in acetone, to be the fastest. Comparatively, its reactivity in MeCN is rather poor. Interestingly, the data also suggest different reaction orders in Me$_8$Fc depending on the catalyst. We tentatively correlate this output with differences in outer

ARTICLE   **Journal Name**

sphere electron transfer efficiencies linked to the steric hindrance around the metal ions either during the $Cu^{II}Cu^{II}$ reduction or for the reduction of the corresponding O_2-adducts. Work including the determination of the rate-limiting step is currently under progress to clarify this point, as we also continue to dissect the structural changes resulting from the solvation of **6** in MeCN in order to understand its inefficiency for ORR. Post catalysis verification that the catalyst(s) are still intact still needs to be optimized since analysis on the crude mixtures are plagued by the presence of Me_8Fc^+, LutH and Lut in large excess that preclude any unambiguous EPR, CV or NMR studies. This may lead us to imagine new architectures and explore the ORR activity of such Cu_2S cores through the prism of the structure-activity relationship that undoubtedly correlates with the fate of the Cu_2/O_2 adduct(s) intermediates formed in the reaction medium.

Author Contributions

Stéphane Torelli and Maylis Orio designed this research and wrote the paper. Jordan Mangue, Jacques Pécaut and Stéphane Torelli performed all the syntheses, characterizations and catalytic studies. Iris Wehrung and Maylis Orio conducted the theoretical calculations. Stephane Torelli, Maylis Orio and Stéphane Ménage discussed this work. All authors have given approval to the final version of the manuscript.

Conflicts of Interest

There are no conflicts to declare.

Acknowledgements

References

1. M. L. Pegis, C. F. Wise, D. J. Martin and J. M. Mayer, *Chem. Rev.*, 2018, **118**, 2340-2391.
2. X. Wang, Z. Li, Y. Qu, T. Yuan, W. Wang, Y. Wu and Y. Li, *Chem*, 2019, **5**, 1486-1511.
3. J. Zhao, C. Fu, K. Ye, Z. Liang, F. Jiang, S. Shen, X. Zhao, L. Ma, Z. Shadike, X. Wang, J. Zhang and K. Jiang, *Nature Communications*, 2022, **13**, 685.
4. R. L. Myers, *The most 100 Most Important Chemical Compounds,*, Greenwood Press, London, 2007.
5. J. M. Campos-Martin, G. Blanco-Brieva and J. L. G. Fierro, *Angew. Chem. Int. Ed.*, 2006, **45**, 6962-6984.
6. C. Chu, Z. Chen, D. Yao, X. Liu, M. Cai and S. Mao, *Angew. Chem. Int. Ed.*, 2024, **63**, e202317214.
7. A. Walawska, M. Olak-Kucharczyk, A. Kaczmarek and M. H. Kudzin, *Materials*, 2024, **17**, 1355. DOI: 10.1039/D4DT01629G
8. A. Ayub, Y. K. Cheong, J. C. Castro, O. Cumberlege and A. Chrysanthou, *Bioengineering*, 2024, **11**, 205.
9. *C&EN Global Enterprise*, 2017, **95**, 32-33.
10. L. Wang, J. Zhang, Y. Zhang, H. Yu, J. Qu and J. Yu, 2022, **18**, e2104561.
11. E. T. Poursaitidis, P. L. Gkizis, I. Triandafillidi and C. G. Kokotos, *Chem. Sci.*, 2024, **15**, 1177-1203.
12. S. Jeon, H. An and Y. Chung, *Sustainable Energy & Fuels*, 2022, **6**, 841-850.
13. M. Melchionna and P. Fornasiero, *Chem*, 2019, **5**, 1927-1928.
14. R. Ciriminna and L. Albanese, 2016, **9**, 3374-3381.
15. T. Devi, Y.-M. Lee, W. Nam and S. Fukuzumi, *Coord. Chem. Rev.*, 2020, **410**, 213219.
16. C. E. Elwell, N. L. Gagnon, B. D. Neisen, D. Dhar, A. D. Spaeth, G. M. Yee and W. B. Tolman, *Chem. Rev.*, 2017, **117**, 2059-2107.
17. S. Fukuzumi, H. Kotani, H. R. Lucas, K. Doi, T. Suenobu, R. L. Peterson and K. D. Karlin, *J. Am. Chem. Soc.*, 2010, **132**, 6874.
18. S. Kakuda, R. L. Peterson, K. Ohkubo, K. D. Karlin and S. Fukuzumi, *J. Am. Chem. Soc.*, 2013, **135**, 6513.
19. M. Langerman and D. G. H. Hetterscheid, *Angew. Chem. Int. Ed.*, 2019, **58**, 12974-12978.
20. H. Kotani, T. Yagi, T. Ishizuka and T. Kojima, *Chem. Commun.*, 2015, **51**, 13385-13388.
21. S. N. Chowdhury, S. Biswas, P. Das, S. Paul and A. N. Biswas, *Inorg. Chem.*, 2020, **59**, 14012-14022.
22. S. Kakuda, C. J. Rolle, K. Ohkubo, M. A. Siegler, K. D. Karlin and S. Fukuzumi, *J. Am. Chem. Soc.*, 2015, **137**, 3330-3337.
23. D. Das, Y.-M. Lee, K. Ohkubo, W. Nam, K. D. Karlin and S. Fukuzumi, *J. Am. Chem. Soc.*, 2013, **135**, 2825-2834.
24. S. N. Chowdhury, S. Biswas, S. Das and A. N. Biswas, *Dalton Trans.*, 2023, **52**, 11581-11590.
25. M. Langerman, M. van Dorth and D. G. H. Hetterscheid, *Eur. J. Inorg. Chem.*, 2023, **26**, e202300218.
26. N. W. G. Smits, D. Rademaker, A. I. Konovalov, M. A. Siegler and D. G. H. Hetterscheid, *Dalton Trans.*, 2022, **51**, 1206-1215.
27. S. D'Agostini, K. G. Kottrup, C. Casadevall, I. Gamba, V. Dantignana, A. Bucci, M. Costas, J. Lloret-Fillol and D. G. H. Hetterscheid, *ACS Catalysis*, 2021, **11**, 2583-2595.
28. N. W. G. Smits, B. van Dijk, I. de Bruin, S. L. T. Groeneveld, M. A. Siegler and D. G. H. Hetterscheid, *Inorg. Chem.*, 2020, **59**, 16398-16409.
29. S. Fukuzumi, L. Tahsini, Y.-M. Lee, K. Ohkubo, W. Nam and K. D. Karlin, *J. Am. Chem. Soc.*, 2012, **134**, 7025-7035.
30. S. Torelli, M. Orio, J. Pécaut, H. Jamet, L. Le Pape and S. Ménage, *Angew. Chem. Int. Ed.*, 2010, **49**, 8249-8252.
31. J. Mangue, C. Gondre, J. Pécaut, C. Duboc, S. Ménage and S. Torelli, *Chem. Commun.*, 2020, **56**, 9636-9639.
32. C. Esmieu, M. Orio, S. Torelli, L. Le Pape, J. Pecaut, C. Lebrun and S. Menage, *Chem. Sci.*, 2014, **5**, 4774-4784.
33. C. Esmieu, M. Orio, J. Mangue, J. Pecaut, S. Menage and S. Torelli, *Chem-Eur J*, 2018, **24**, 5060-5063.
34. M. Gennari, D. Brazzolotto, J. Pécaut, M. V. Cherrier, C. J. Pollock, S. DeBeer, M. Retegan, D. A. Pantazis, F. Neese, M. Rouzières, R. Clérac and C. Duboc, *J. Am. Chem. Soc.*, 2015, **137**, 8644-8653.

Dalton Transactions Accepted Manuscript

35. C. Matsubara, N. Kawamoto and K. Takamura, *Analyst*, 1992, **117**, 1781-1784.
36. K. Takamura, C. Matsubara and T. Matsumoto, *Anal Sci*, 2008, **24**, 401-404.
37. M. L. Skavenborg, M. S. Møller, C. J. Miller, J. Hjelm, T. D. Waite and C. J. McKenzie, *Inorg. Chem.*, 2023, **62**, 18219-18227.
38. C. J. M. van der Ham, D. N. H. Zwagerman, L. Wu, J. P. Hofmann and D. G. H. Hetterscheid, *ChemElectroChem*, 2022, **9**, e202101365.
39. B. van Dijk, J. P. Hofmann and D. G. H. Hetterscheid, *Phys. Chem. Chem. Phys.*, 2018, **20**, 19625-19634.
40. M. L. Pegis, B. A. McKeown, N. Kumar, K. Lang, D. J. Wasylenko, X. P. Zhang, S. Raugei and J. M. Mayer, *ACS Central Science*, 2016, **2**, 850-856.

Dalton Transactions Accepted Manuscript

DATA AVAILABILITY STATEMENTS for

Copper complexes with Cu₂S cores: (Solvent)Effects on Oxygen Reduction Reactions.

By

Jordan Mangue,[a] Iris Wehrung,[b] Jacques Pécaut,[c] Stéphane Ménage,[a] Maylis Orio[*b] and

Stéphane Torellil[*a]

The data supporting this article have been included as part of the Supplementary Information.

Crystallographic data for **6** and **II** have been deposited at the CCDC under 2347081 and 2347077, respectively and can be obtained from https://www.ccdc.cam.ac.uk/